DRAFT VERSION AUGUST 25, 2025
Typeset using LaTeX **twocolumn** style in AASTeX7.0.1

A Photometric Analysis of SN 1983V

SOPHIA S. KRESSY [1] AND ORI FOX [2]

[1] *Department of Physics and Astronomy, University of North Carolina Chapel Hill, Chapel Hill, NC 27599*
[2] *Space Telescope Science Institute*

(Received TBD; Revised TBD; Accepted TBD)

Submitted to The Astrophysical Journal

ABSTRACT

We present a photometric analysis for supernova 1983V, a Type Ic that exploded ∼39 years ago in galaxy NGC 1365 We reduce and align *JWST MIRI* and *NIRCam* images using `JWHASP`, a *JWST* to *HST* alignment and calibration pipeline. A PSF is fitted for each filter and the magnitude and flux are derived. We fit a dust model to the resulting SED and found that SN 1983V most likely contains a hot and cold dust component. Our dust model estimates the total dust mass of the supernova to be $0.01 M_{\odot}$. This finding falls inline with the current thinking that dust abundance increases with days post discovery. We solve for the blackbody radius and expansion velocity as well, and find uniquely small numbers, suggesting that assumptions in dust geometry applied may be incorrect. However, we find that there is not enough data to sufficiently conclude the origins and geometry of the dust in SN 1983V, and that further observations are required.

Keywords: Type Ic supernovae (1730) — Core-collapse supernovae (304) — Supernova dynamics (1664) — James Webb Space Telescope (2291) — Circumstellar dust (236)

1. INTRODUCTION

Large quantities of dust have been observed in high-redshift galaxies (R. Maiolino et al. 2004). Core-Collapse Supernovae (CCSNe) may be responsible for this dust (F. Cernuschi et al. 1967; F. Hoyle & N. C. Wickramasinghe 1970). Simulations of expanding Type IIP ejecta in the ISM have shown to produce sufficient dust to account for the quantities observed (P. Todini & A. Ferrara 2001; T. Nozawa et al. 2003, 2008). However, *Spitzer* has previously observed CCSNe and found dust masses 2-3 orders of magnitude too small to account for this dust at high redshifts (C. L. Gerardy et al. 2002; M. Pozzo et al. 2004; B. E. K. Sugerman et al. 2006; W. P. S. Meikle et al. 2007, 2011; J. E. Andrews et al. 2010, 2011; J. Fabbri et al. 2011; T. Szalai et al. 2011). This could be due in part to the range of *Spitzer* 's wavelength coverage. Specifically, *Spitzer* 's only had access to 3.6μm and 4.5μm imaging after 2008. These wavelengths trace the hottest dust (>500K), but is not able to detect warm and cold dust reservoirs (R. Wesson et al. 2015).

JWST 's *MIRI* and *NIRCam* may provide a solution to detecting warm and cold dust. *JWST NIRCam* varies from 0.6μm - 5μm and *MIRI* covers 5μm to 28μm . *MIRI* specifically will be able to observe colder dust not previously accessible (20μm ≈150K). Previous SNe studies have primarily detected hot dust <1 year post-explosion [CITE]. Colder dust in older SNe will now be accessible, and *JWST* will help fill the "days post-discovery" gap [CITE]. This will better constrain and inform dust masses and models.

JWST data is being released on a daily basis of archival supernovae previously observed by Hubble. Recently, *JWST* has uncovered some of the largest ever supernova (SN) dust masses in SNe Type IIp 2004et (M. Shahbandeh et al. 2023) and SNe Type IIn 2005ip (M. Shahbandeh et al. 2025).

Various models have been produced to explain the dust quantities seen. Some models suggest slow and steady dust creation over 10,000 days (R. Wesson et al. 2015; R. Wesson & A. Bevan 2021). Others suggest that dust creation does not begin until >5 yrs post-explosion (C. Gall et al. 2014). Rapid dust growth, which is only now, at later epochs, visible due to optical depth effects, has also bee suggested (A. Sarangi & I. Cherchneff 2013; E. Dwek et al. 2019). *Spitzer* has shown that SNe dust can remain bright for many years post-explosion, possibly from shock interaction with CircumStellar Material (CSM) [CITE]. This contradicted models where only some progenitors produce dusty CSM/ejecta.

Email: skressy@email.unc.edu

JWST /*MIRI* will be able to probe this warm and cold dust at longer wavelengths, not previously accessible (G. Hosseinzadeh et al. 2022).

In this paper we present *JWST* data from *MIRI* and *NIRCam* for SN 1983V. Supernova 1983V was first discovered by R.O. Evans in NGC 1365 on 25 November 1983. Figure 1 shows the approximate location of SN 1983V in NGC 1365 observed by *HST* as apart of the PHANGs survey [CITE]. It was observed by J. C. Wheeler et al. (1987) 13 days post discovery, who found a spectra similar to Type Ib, but with less He and more C and O in the ejecta. Later on, A. Clocchiatti et al. (1997) observed 1983V with CCD photometry and low-resolution spectra. They found a lack of evidence of HI, HeI, or SiII near max light, and thus categorized 1983V as a Type Ic SNe. A. Clocchiatti et al. (1997) suggested that 1983V could be an extreme case of a stripped He/H envelope, due to a lack of H in optical spectrum and little to nonexistent He. A. Clocchiatti et al. (1997) goes on to categorize 1983V as a Type Ic subclass – it's light curve decays rapidly, then the rate decreases and exponentially decays. This is referred to as the 'slow' Type Ic subclass. This differs from other subclasses of Type Ic, where the light curve decays rapidly and does not follow a common locus. The distance to SN 1983V has been reported as 0.0054 redshift (M. Modjaz et al. 2016).

In this paper we present a photometric analysis of SN 1983V. *JWST MIRI* and *NIRCam* images are aligned and reprocessed (Section 2). Photometry is then done on these images (Section 3) to extract fluxes for SN 1983V. We produce an SED and fit dust models and discuss possible geometric implications (Section 4). We fit hot and cold dust components to the SED for silicate and carbon compositions, respectively, and find that SN 1983V has a dust mass of $\approx 0.01\ M_\odot$. The geometric and evolutionary implications of these findings are then discussed (Section 5). Summary of findings are presented in Section 7.

2. JWST OBSERVATIONS

SN 1983V was observed as part of the Cycle 1 General Observers (GO) 2107 program (PI J. Lee). Images of SN 1983V were taken with the *JWST* Mid-Infrared Instrument (MIRI; [Bouchet et al 2015; Ressler et al. 2015, Rieke et al. 2015; Rieke and Wright 2022] and Near-Infrared Camera (NIRCam; CITE) on Aug. 13th 2022 (X days post-explosion). JWST *NIRCam* and *MIRI* observations of 1983V were downloaded via MAST. Observations in *NIRCam* covered F770W, F1000W, F1130W, F2100W, and in *MIRI* bands covered F200W, F300M, F335M, F360M. The FASTR1 readout pattern in the FULL array mode and a 4-point extended source dither pattern was used. The data were processed with the JWST Calibration Pipeline version 1.7.2, using the Calibration Reference Data System version 11.16.9. Table 1 lists the instrument, filter, exposure and integration times.

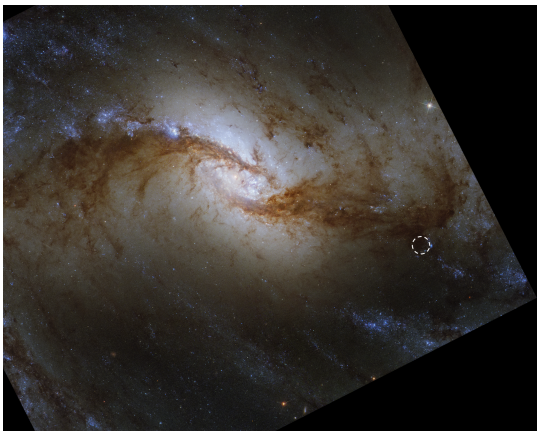

Figure 1. The NGC 1365 galaxy, home to SN 1983V, observed by Hubble. SN 1983V approximate location is noted with the dashed circle. An optically thick cloud is blocking optical light from the 1983V from appearing, but appears brightly in mid-infrared (see Figure 3). Credit NASA, ESA, CSA, STScI, Janice Lee (STScI), Thomas Williams (Oxford), PHANGS Team

The James Webb Hubble Aligned Supernova Photometry (JWHASP) pipeline was used reprocess and align *JWST* observations to previous *HST* data for SN1983V's position. *MIRI* and *NIRCam* raw images were inputs to the pipeline. In an initial step, the images were calibrated to the ramp data and the countrate data, producing 'Level 1' data images. To address cosmic rays, calibrated images for each filter were cosmic ray flagged. A "background image" was constructed for each filter by taking a sigma-clipped average of the individual dithers in each detector coordinates, and this background was then subtracted from the calibrated ('Level 2') individual dither images in the corresponding filter. The images were aligned with the *JWST* software JHAT [CITE]. The background-subtracted level-two images were then mosaicked into a single calibrated image for each filter (see Figure 2 [Bright and JWST/MIRI Team 2016; Greenfield and Miller 2016; Bushhouse et al 2022].

Figure 2 shows *JWST* observations, from *MIRI* and *NIRCam* , of SN 1983V for all filters. The top row displays *NIRCam* observations in F200W, F300M, F335M, and F360M from left to right, respectively. The bottom row displays *MIRI* observations in F770W, F1000W, F1130W, and F2100W from left to right, respectively. The panels are centered on SN 1983V. It appears than in the NIR, SN 1983V is nearly gone. Meanwhile, in the *MIRI* filters, the SN appears most clearly in F1000W and F1130W. At longer wavelengths, the SN also appears bright, but a close, presumably dusty, source begins to interfere. In F2100W, the SN and it's neighbor blend together. The increase in flux at Mid-IR wavelengths suggests there may be heated dust emission.

Table 1. JWST Observations

Instrument	Filter	Effective Exposure [s]	Effective Integration Time [s]
NIRCam	F200W	2405.03	53.684
NIRCam	F300M	773.04	96.631
NIRCam	F335M	773.04	96.631
NIRCam	F360M	858.94	53.684
MIRI	F770W	532.79	22.2
MIRI	F1000W	532.79	22.2
MIRI	F1130W	532.79	22.2
MIRI	F2100W	532.79	22.2

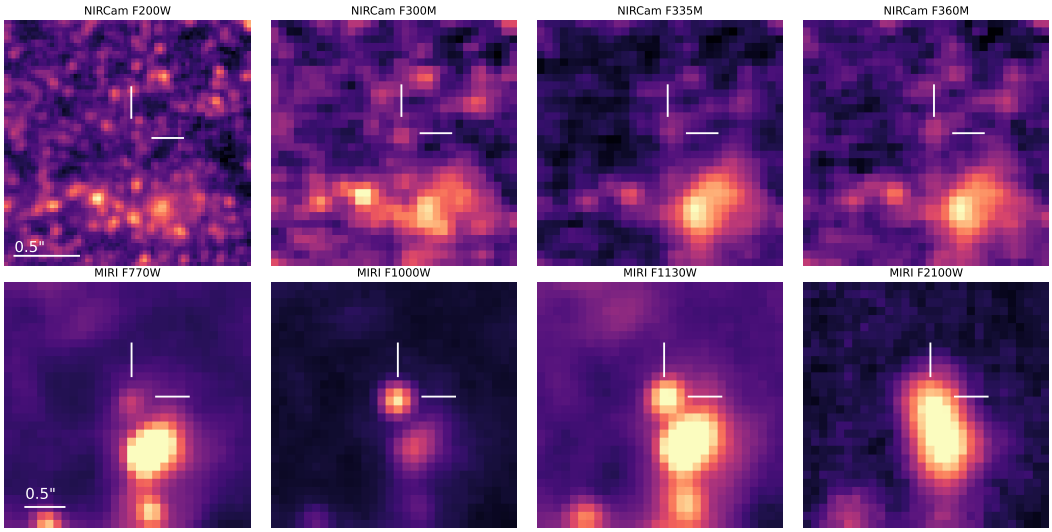

Figure 2. *MIRI* /*NIRCam* observations of SN 1983V for all filters.

MIRI observed in four filters – F770W, F1000W, F1130W, and F2100W, which in Figure 3, are overlaid in colors corresponding to their relative wavelengths. F2100W corresponds to red, F1130W is orange, F1000W is green, F770W is blue. The large, left panel shows the majority of the *MIRI* observation, encompassing most of NGC 1365. SN 1983V is found in the spiral arm of the galaxy, typical of Type Ic SNe. The zoomed-in panel on the right shows SN 1983V in detail. The longer wavelengths (F1130W, F2100W) colors (orange, red) produce a haze around the SN, suggesting that these wavelength are picking up dust emission.

Similar to Figure 3, Figure 4 shows *NIRCam* observations in four filters – F200W, F300M, F335M, F360M – overlaid in corresponding colors relative to wavelength. The right zoomed-in panel shows SN 1983V located, and appears far dimmer at these shorter wavelengths, although a source is noticeable.

3. PHOTOMETRY

Photometry was conducted on the *JWST* images to derive fluxes for the supernova. The publicly available photometric analysis code `space_phot` by Justin Pierel was employed for *MIRI* and *NIRCam* observations. To measure the brightness of the SN, for each filter the supernova was centroided and point-spread-function (PSF) photometry was performed using `WebbPSF` (M. D. Perrin et al. 2014). The flux was calibrated by applying flux offsets by measuring the PSF of all stars in the field and comparing them to corresponding catalogs created by the pipeline. The fluxes of all four dithers for each filter were then averaged.

To establish quality of calibration, the residual is calculated between the model (the PSF) and raw data. The model result and residual varied greatly depending on the background scaling, fit width, and centroid position of x and y, so a 'goodness of fit' parameter was necessary. This was done by first modeling the residual with a 2D 'surface' polynomial, effec-

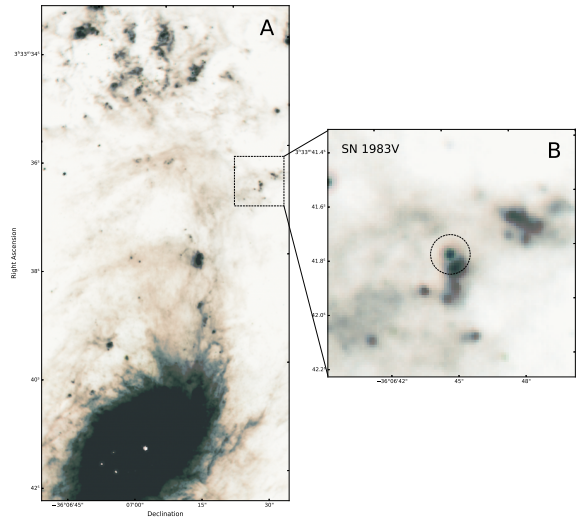

Figure 3. Observation of NGC 1365 with zoom-in box on SN 1983V from *JWST /MIRI* images

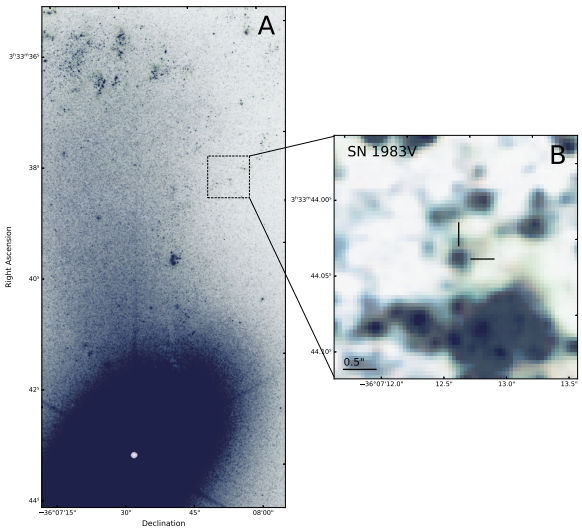

Figure 4. Observation of NGC 1365 with zoom-in box on SN 1983V from *JWST /NIRCam* images

tively locating any lasting high noise objects and leaving only background noise. Then, a second, or 'background' residual is found between the 2D polynomial model and the PSF residual. Finally, the standard deviation of the 'background' residual was found and used as a minimization parameter. A small standard deviation suggests a smaller range of signal, and therefore a lack of signal and only background noise leftover. This can also be taken to mean that the PSF and 2D polynomial models fit well and removed all signal. As the 2D polynomial model parameters are constant, the PSF model parameters can be varied until the minimum standard deviation is located. Thus, these PSF model parameters are then used to find the optimal photometry of the supernova point source.

Figure 5 show the photometry for optimized fit parameters for the *MIRI* filters F770W, F1000W, F1130W, F2100W, from top to bottom. PSF model parameters include background, fit width and x and y centroid positions, which were varied across parameter space and then optimized using the standard deviation of the 'background' residual. As seen in the far-right panel, the residual lacks the majority of the noise of the supernova, which is modeled in the fourth panel label 'BKG+Model'.

From Figure 5, the magnitude is found from the PSF fit, which can then be covered to flux in Janksys with,

$$\mathrm{F} = 10^{-0.4(\mathrm{M_{abs}}+48.6)} * 1 \times 10^{23}. \quad (1)$$

Table 2 reports the magnitude, magnitude error, flux and flux error for each filter for both *MIRI* and *NIRCam* . Magnitudes are the absolute (?) magnitudes and fluxes are in Janksys.

4. ANALYSIS

4.1. *Dust Modeling*

An SED can be created from the fluxes derived from the photometry results (see Figure 6). The SED was fit by assuming that dust can be modeled by a blackbody emission spectrum. The modeling took into account dust characteristics such as dust grain size and composition.

In the case of SN 1983V, a two component (hot and cold) dust model was assumed. A hot component made of silicate and a cold component made of carbon were modeled and fitted to the SED. A dust grain size of $0.1\mu m$ was assumed. Figure 6 displays the dust modeling results. The SED points are plotted in black, while the full dust model is overlaid in green, containing both hot (red, dotted) and cold (blue, dotted) dust components. The resulting mass and temperatures for each component are displayed in the legend in the lower right corner. The fitted cold component was found to have a temperature of 170K and $0.01\mathrm{M}_{\odot}$, and the hot component 524K and 6.4×10^{-6}. The total filter integrated dust mass was found to be $0.01\mathrm{M}_{\odot}$. The hot component contributes very little to the overall dust mass, with the cold component acting as the main determinate. These parameters are also listed in Table 3.

In the dust modeling fit, *NIRCam* measurements are shorter wavelengths ($< 5\mu\mathrm{m}$), and trace the hotter dust. *MIRI* is represented by the longer wavelengths ($> 5\mu\mathrm{m}$). The F770W - F1000W include the peak seen in the hot component as well as the cold component. The F2100W or $21\mu m$ measurement is entirely determined by the cold component and has the effect of constraining the amount of cold dust, and therefore the total dust.

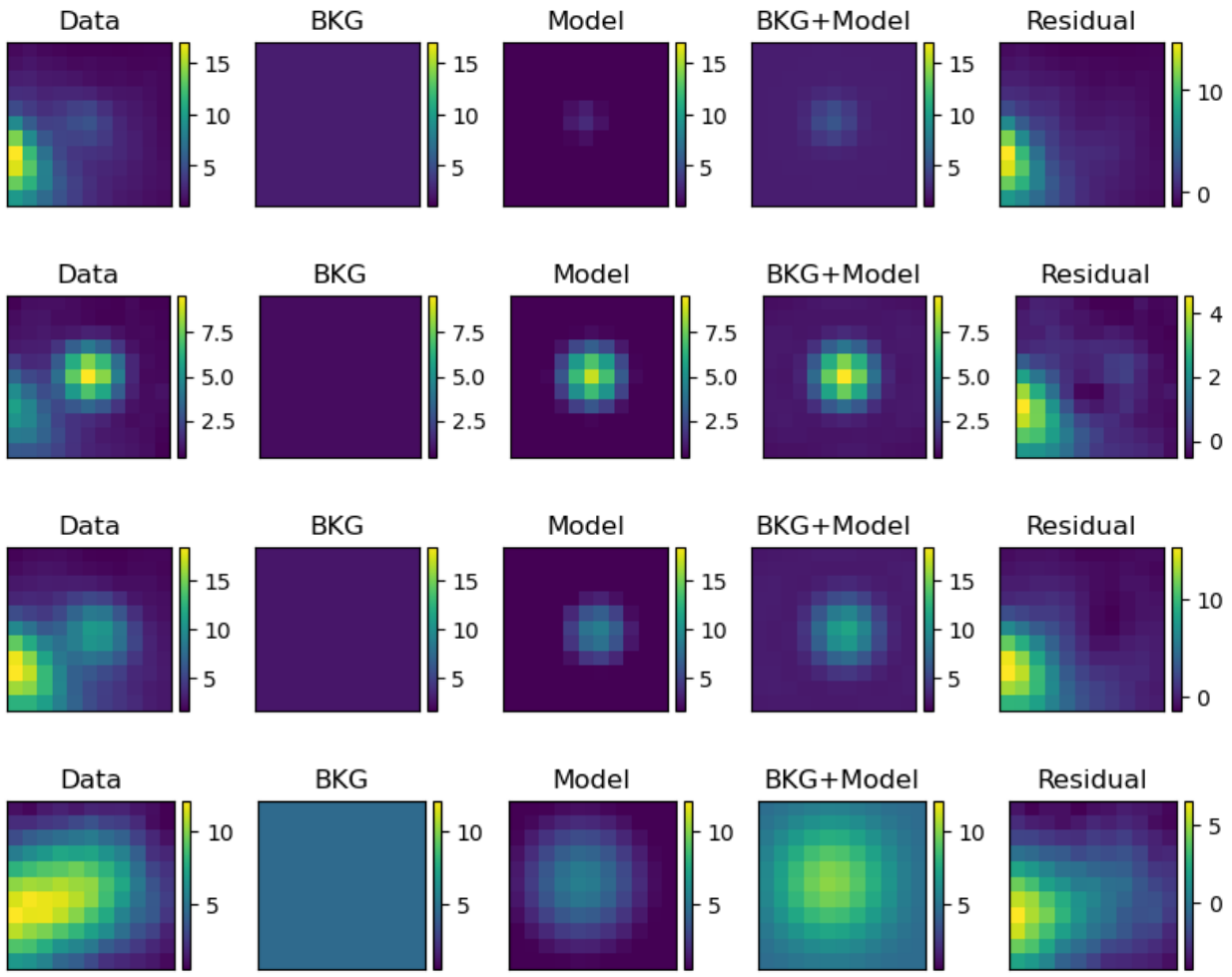

Figure 5. Photometry of the four *MIRI* filters for optimized fit parameters. Top to bottom: F770W, F1000W, F1130W, and F2100W. From left to right, panels show the data, the background value (constant), the PSF model, the combined background and PSF model, and the residual between the data and the background and model. For each filter, the panels share the same intensity scale, except the background and model panel. Optimal parameters were chosen by minimizing the standard deviation of the 'background' residual. In this way, photometry results are reproducible and provide systematic error on the fit.

Figure 7 shows the found dust mass for SN 1983V in context with other SN findings previously reported. SN 1983V is denoted with the yoda head symbol, at 39 years post explosion, making it the oldest SN with measurement dust mass. Other SNe are denoted with their specific marker (see legend) with some SNe having multiple dust measurements overtime (connecting lines). One sigma uncertainty is plotted as the gray shaded region. Overall, there is a positive correlated trend between days since explosion and total dust mass. SN 1983V may show the slope of this relationship is not as steep as previously reported, but additional later time SNe dust measurements are needed.

SN 1983V is one of the largest dust masses reported to date of $0.01 M_{\odot}$. However, the mass reported is the lower-limit. There very well could be colder dust that is only accessible at longer wavelengths (¿$21 \mu m$). Thus, in Figure 7, the upward arrows from SNe markers indicate that it is a lower limit.

4.2. *Blackbody Radius*

From the fitted dust mass and temperature parameters, the total integrated luminosity can be found. Similar to treatment in M. Shahbandeh et al. (2023), we assume the dust in SN ejecta is approximated by a homogeneous expanding sphere. If we treat each dust grain as a blackbody, then a sphere of geometrically oriented grains can also be treated as a uniform blackbody. The blackbody radius is then the minimum radius of this dust sphere. The radius can be found by first calculating the total integrated luminosity (L_{tot}) from the photometric flux ($F(\lambda)$),

$$L_{tot} = \int F(\lambda) d\lambda \cdot 4\pi d^2. \quad (2)$$

(3)

Table 2. Photometry

Instrument	Filter	Magnitude	eMag	Flux [Jy]	eFlux [Jy]
NIRCam	F200W	27.45	0.58	3.79×10^{-8}	2.05×10^{-8}
NIRCam	F300M	25.96	0.43	1.48×10^{-7}	5.94×10^{-8}
NIRCam	F335M	25.42	0.26	2.45×10^{-7}	5.91×10^{-8}
NIRCam	F360M	25.68	0.45	1.93×10^{-7}	8.14×10^{-8}
MIRI	F770W	21.36	0.05	1.03×10^{-5}	5.43×10^{-7}
MIRI	F1000W	19.85	0.01	4.15×10^{-5}	6.49×10^{-7}
MIRI	F1130W	19.59	0.01	5.25×10^{-5}	7.78×10^{-7}
MIRI	F2100W	18.96	0.02	9.40×10^{-5}	1.85×10^{-6}

Table 3. Fitted Parameters

Dust Component	Composition	M_{dust} [$M_\odot$]	T_{dust} [K]
Hot	Silicate	$6.4\times10^{-6}\pm1.65\times10^{-6}$	524±29
Cold	Carbon	0.01 ± 0.00	170±2.5

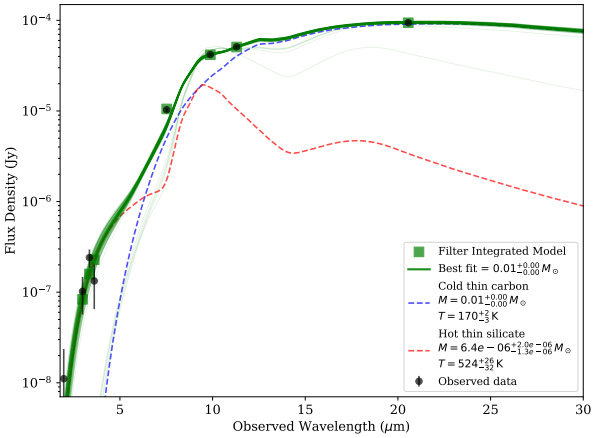

Figure 6. A two component dust model was fitted to the SN's SED. The green line shows the integrated dust model of two models – hot and cold dust components. The hot dust model is plotted in dashed red, and the cold dust model is plotted in dashed blue. The black points indicate the SED points at each filter, including error bars. The resulting dust mass and temperature for both dust components, as well as the total integrated model dust mass, is displayed in the legend in the right bottom corner.

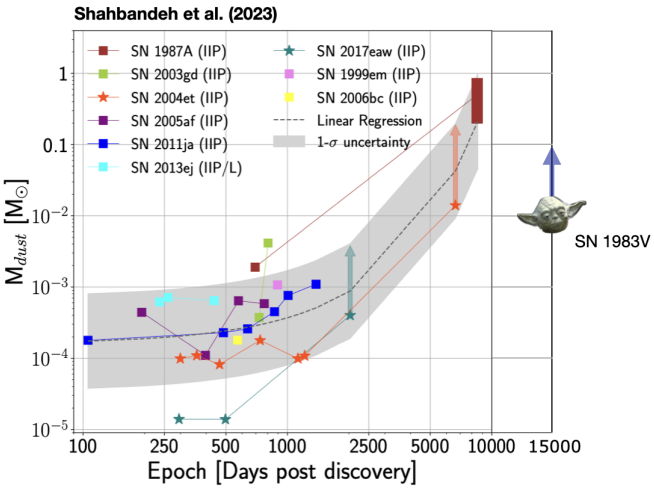

Figure 7. A reproduction from (M. Shahbandeh et al. 2023), the total dust mass of recorded supernovae versus time is shown. The point for SN 1983V is denoted with Yoda's head. A trend of increasing total dust mass for increasing time is apparent. This may suggest that dust is now visible some years later, or that dust is forming new.

The blackbody radius is then,

$$r_{bb} = \sqrt{\frac{L_{tot}}{4\pi\sigma T^4}} \quad (4)$$

$$r_{bb} = \sqrt{\frac{\int F(\lambda)d\lambda \cdot 4\pi d^2}{4\pi\sigma T^4}}. \quad (5)$$

Table 4 reports the total integrated luminosity for each dust component independently, using values from Table 3. Table 4 also lists the blackbody radius (r_{bb}), and the expansion velocity (ν_{exp}). The expansion velocity is found by $\nu_{bb} = r_{bb}/t$, where t is the time from explosion to observation date (≈39 yrs).

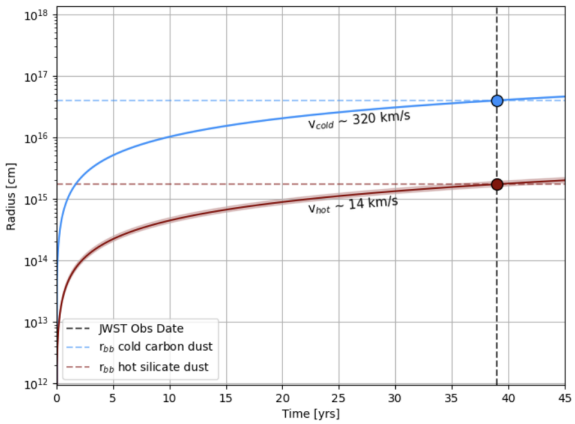

Figure 8. Time since explosion is plotted in days on the x-axis, with blackbody radius in cm plotted on the y-axis. The blackbody radius for each component is plotted as points. The derived expansion velocity is plotted across time since explosion.

Figure 8 shows the blackbody radius versus time in days, producing the expansion velocity. Expansion velocities are shown for the hot (red) and cold (blue) dust components, and gives their velocities at observation ∼39 years later – 14 km/s and 320 km/s for hot and cold components, respectively. Even at 39 years post-explosion, expansion velocities of these values are extremely low. Knowing that the blackbody radius is a minimum suggest that these velocities are also at the lower limit. However, there remains the possibility that our assumptions are incorrect in modeling dust as a blackbody, such as geometry of the dust grains. Non-spherical dust geometries could greatly affect the total dust mass or blackbody radius. Regardless, that is beyond the scope of this work and will need to be investigated in the future.

5. DISCUSSION

5.1. *Physical Scenarios*

5.2. *Dust Origin and Heating Mechanisms*

6. NEXT STEPS

Here we have presented the beginnings of findings for SN 1983V. More JWST, specifically MIRI, observations are needed to understand the full scope of dust creation in SN 1983V. Currently, only 4/9 MIRI filters are recorded for 1983V. Increasing data points as well as including filters F1280W, F1500W, F1800W would constrain dust parameters greatly. These filters specifically would trace colder dust, which we rely on F2100W greatly for, and inform us on the quality of our cold dust model. As the cold dust dominates the overall dust mass, these filters would have a large impact on this papers findings. Additionally, filter F2550W would inform us of even colder dust that we have not probed yet, and thus may increase our total dust mass and give a more accurate picture.

New spectra of SN1983V would also increase our overall understanding of the supernovae. Chemical abundances and composition from spectra would help to unveil the stripped envelope nature and possibly the progenitor of 1983V. Interactions with the CSM may also be revealed. Velocities would provide a geometric and evolutionary perspective as well.

7. SUMMARY

8. ACKNOWLEDGMENTS

We acknowledge and thank the Kavli Summer Program in Astrophysics for the opportunity to collaborate and thank Shazrene Mohammed for organizing this years program at University of Virginia.

This work has been supported by the Future Investigators in NASA Earth Science and Space Science and Technology (FINESST) grant.

REFERENCES

Andrews, J. E., Gallagher, J. S., Clayton, G. C., et al. 2010, ApJ, 715, 541, doi: 10.1088/0004-637X/715/1/541

Andrews, J. E., Clayton, G. C., Wesson, R., et al. 2011, AJ, 142, 45, doi: 10.1088/0004-6256/142/2/45

Cernuschi, F., Marsicano, F., & Codina, S. 1967, Annales d'Astrophysique, 30, 1039

Clocchiatti, A., Wheeler, J. C., Phillips, M. M., et al. 1997, ApJ, 483, 675, doi: 10.1086/304268

Dwek, E., Sarangi, A., & Arendt, R. G. 2019, ApJL, 871, L33, doi: 10.3847/2041-8213/aaf9a8

Fabbri, J., Otsuka, M., Barlow, M. J., et al. 2011, MNRAS, 418, 1285, doi: 10.1111/j.1365-2966.2011.19577.x

Table 4. Modeled Dust Parameters

Dust Component	Composition	L_{tot} [erg s^{-1}]	r_{bb} [cm]	ν_{exp} [km s^{-1}]
Hot	Silicate	5.37×10^{37}	9.97×10^{14}	8.10
Cold	Carbon	3.09×10^{38}	2.28×10^{16}	185.64

Gall, C., Hjorth, J., Watson, D., et al. 2014, Nature, 511, 326, doi: 10.1038/nature13558

Gerardy, C. L., Fesen, R. A., Nomoto, K., et al. 2002, ApJ, 575, 1007, doi: 10.1086/341430

Hosseinzadeh, G., Sand, D. J., Lundqvist, P., et al. 2022, ApJL, 933, L45, doi: 10.3847/2041-8213/ac7cef

Hoyle, F., & Wickramasinghe, N. C. 1970, Nature, 226, 62, doi: 10.1038/226062a0

Maiolino, R., Schneider, R., Oliva, E., et al. 2004, Nature, 431, 533, doi: 10.1038/nature02930

Meikle, W. P. S., Mattila, S., Pastorello, A., et al. 2007, ApJ, 665, 608, doi: 10.1086/519733

Meikle, W. P. S., Kotak, R., Farrah, D., et al. 2011, ApJ, 732, 109, doi: 10.1088/0004-637X/732/2/109

Modjaz, M., Liu, Y. Q., Bianco, F. B., & Graur, O. 2016, ApJ, 832, 108, doi: 10.3847/0004-637X/832/2/108

Nozawa, T., Kozasa, T., Umeda, H., Maeda, K., & Nomoto, K. 2003, ApJ, 598, 785, doi: 10.1086/379011

Nozawa, T., Kozasa, T., Tominaga, N., et al. 2008, ApJ, 684, 1343, doi: 10.1086/589961

Perrin, M. D., Sivaramakrishnan, A., Lajoie, C.-P., et al. 2014, in Society of Photo-Optical Instrumentation Engineers (SPIE) Conference Series, Vol. 9143, Space Telescopes and Instrumentation 2014: Optical, Infrared, and Millimeter Wave, ed. J. M. Oschmann, Jr., M. Clampin, G. G. Fazio, & H. A. MacEwen, 91433X, doi: 10.1117/12.2056689

Pozzo, M., Meikle, W. P. S., Fassia, A., et al. 2004, MNRAS, 352, 457, doi: 10.1111/j.1365-2966.2004.07951.x

Sarangi, A., & Cherchneff, I. 2013, ApJ, 776, 107, doi: 10.1088/0004-637X/776/2/107

Shahbandeh, M., Sarangi, A., Temim, T., et al. 2023, MNRAS, 523, 6048, doi: 10.1093/mnras/stad1681

Shahbandeh, M., Fox, O. D., Temim, T., et al. 2025, ApJ, 985, 262, doi: 10.3847/1538-4357/adce77

Sugerman, B. E. K., Ercolano, B., Barlow, M. J., et al. 2006, Science, 313, 196, doi: 10.1126/science.1128131

Szalai, T., Vinkó, J., Balog, Z., et al. 2011, A&A, 527, A61, doi: 10.1051/0004-6361/201015624

Todini, P., & Ferrara, A. 2001, MNRAS, 325, 726, doi: 10.1046/j.1365-8711.2001.04486.x

Wesson, R., Barlow, M. J., Matsuura, M., & Ercolano, B. 2015, MNRAS, 446, 2089, doi: 10.1093/mnras/stu2250

Wesson, R., & Bevan, A. 2021, ApJ, 923, 148, doi: 10.3847/1538-4357/ac2eb8

Wheeler, J. C., Harkness, R. P., Barker, E. S., Cochran, A. L., & Wills, D. 1987, ApJL, 313, L69, doi: 10.1086/184833